The effect of oxygen partial pressure on dislocation creep in polycrystalline uranium dioxide

Philippe Garcia, Audrey Miard, Thomas Helfer, Jean-Baptiste Parise, Xavière Iltis, Guy Antou

HAL Id: hal-03281685

https://unilim.hal.science/hal-03281685

Submitted on 15 Dec 2022

The effect of oxygen partial pressure on dislocation creep in polycrystalline uranium dioxide

Philippe Garcia[a], Audrey Miard[a], Thomas Helfer[a], Jean-Baptiste Parise[a], Xavière Iltis[a], Guy Antou[b]

[a]*CEA, DES, IRESNE, DEC, Cadarache F-13108 Saint-Paul-Lez-Durance, France*
[b]*Univ. Limoges, CNRS, IRCER, UMR 7315, F-87000 Limoges, France*

Abstract

We report a set of compression test experiments carried out on sintered uranium dioxide at 1500°C, at constant strain rates and under controlled oxygen partial pressures. The macroscopic data indicate an initial strain hardening stage followed by a quasi steady–state period during which changes in the stress level are sluggish. The data are further interpreted in a continuum mechanics, finite strain framework, in both one and two–dimensional geometries, whence stress and oxygen partial pressure exponents of the creep law are estimated. The stress exponent is indicative of power–law creep. The oxygen partial pressure exponent is consistent with a strain–rate limited by vacancy mediated self–diffusion of the slowest moving ion, suggesting a climb–controlled recovery process. Some samples are further characterized using SEM/EBSD which reveals signs of plastic deformation typical of recovery creep. The effect of oxygen pressure upon microstructure is discussed.

Keywords: uranium dioxide, non–stoichiometry, creep, self-diffusion, defect behaviour
PACS: 62.20.Hg, 61.72.Hh, 66.30.-h, 66.30.Lw, 02.70.Dh, 61.05.J-

1. Introduction

Creep is an important property for nuclear fuels as it is essential for predicting the complex thermomechanical behaviour of fuel rods particularly in the event of Pellet Cladding Mechanical Interaction, *i.e.* at high temperature and stress. In polycristalline uranium dioxide, it has therefore been the object of numerous studies but there still remains some ambiguity as to what actual deformation mechanisms and rate limiting phenomena prevail.

Email addresses: `philippe.garcia@cea.fr` (Philippe Garcia), `audrey.miard@cea.fr` (Audrey Miard), `thomas.helfer@cea.fr` (Thomas Helfer), `jean-baptiste.parise@cea.fr` (Jean-Baptiste Parise), `xaviere.iltis@cea.fr` (Xavière Iltis), `guy.antou@unilim.fr` (Guy Antou)

The majority of studies relating to the stoichiometric material have involved exposing it to reducing conditions, generally a mixture of argon and hydrogen. Authors argue it is a guarantee for maintaining a constant chemical composition[37, 38, 15, 35]. Although the oxygen to metal ratio will indeed remain close to 2 under those conditions, the oxygen activity is liable to change over several oders of magnitude depending for example upon the level of residual humidity. Therefore in this study, oxygen partial pressure is considered just as any other environmental intensive thermodynamic variable. The main advantage of this lies in that, in non stoichiometric oxides, the oxygen partial pressure dependence of many properties reflects the existence of equilibria between point defects thus providing insight into the mechanisms involved[16].

This work is an attempt at determining whether creep mechanisms in UO_{2+x} are related to cation diffusion properties. Small deviations from stoichiometry in the dislocation creep regime are studied by carrying out compression test experiments on sintered pellets at $1500°C$, at two constant strain rates, and at different oxygen partial pressures. There are several aspects to this work which, combined, differentiate it from previous similar studies. The first is the effort to carry out measurements under controlled and measured oxygen pressures. The second lies in the fact that we have chosen to analyse results in the light of a kinematic hardening model using a finite strain formalism, in one and two-dimensional geometries. Finally, we have used EBSD to characterise some of the effects creep has on the microstructure.

The first part of this study (section 2), describes the materials and creep tests performed, with a particular attention given to the control of the oxygen partial pressure. Section 3 concerns the modelling hypotheses. We present and justify the material behaviour law we have adopted along with the one and two dimensional models set up. Section 4 is devoted to the entire set of results. These involve results of macroscopic tests and their analysis with a viscoplastic model. The main microstructural features observed are also presented in this section. They are obtained from Electron Back-Scatter Diffraction (EBSD) characterisations of polished sample sections following compression tests. A comprehensive discussion is proposed in section 5 based on the stress and oxygen partial pressure exponents derived and on the effect of compression tests on microstructures. Our results are discussed in the light of previous studies.

2. Experimental

2.1. Material manufacturing and characteristics.

The materials studied are polycrystalline uranium dioxide pellets. They were manufactured from powders which were cold pressed at 400 MPa and further sintered at $1670°C \pm 20°C$ for four hours in pure hydrogen. The sintered pellets are 8.19 mm in diameter and approximately 16 mm in height. The rather high height to diameter ratio is intended to minimize multiaxial effects due to friction at interfaces between the pellets and tungsten plates between which they are clamped during the compression test.

Test number	Crosshead speed (μm/min.)	Approximate linear strain rate (s^{-1})	Oxygen pressure (atm.)	Duration (mins)	Final linear deformation (%)
1	20	2×10^{-5}	1.3×10^{-12}	126	13.1
2	20	2×10^{-5}	1.1×10^{-11}	123	13.1
3	20	2×10^{-5}	1.3×10^{-11}	129	13.2
4	20	2×10^{-5}	4.8×10^{-11}	127	13.8
5	20	2×10^{-5}	7.3×10^{-11}	130	14.0
6	50	5×10^{-5}	4.0×10^{-13}	63	17.2
7	50	5×10^{-5}	1.3×10^{-12}	60	16.2
8	50	5×10^{-5}	2.4×10^{-12}	61	16.6
9	50	5×10^{-5}	5.3×10^{-12}	62	17.1

Table 1: Conditions of tests carried out

The pellets' microstruture is characterized by a high density of essentially closed micron scale porosity (mainly intragranular pores with an average diameter of 0.4 μm representing a volume fraction of 1.8 ± 0.1%) and a median grain size of roughly 13 μm with a broad size distribution (10 % of grains have an apparent diameter of less than 6 μm and 90 % an apparent diameter of less than 24 μm). A more detailed characterisation of the as-manufactured microstructure is provided elsewhere[3].

2.2. Creep experiments

Creep experiments are carried out using a compression test machine which comprises an 100 kN INSTRON frame equipped with a tungsten furnace capable of uniformly heating the region in which the pellet is placed to a maximum temperature of approximately 1700°C (see [38, 35] for instance for details).

The pellets are placed upon a tungsten plate itself resting on an vertical column clamped at its lower end. The force of the upper column is transmitted through a second tungsten plate placed on the top part of the pellet. The system is also equipped with a load cell placed at the top of the load column along with a displacement gauge for controlling the crosshead movement. In addition to these devices, two LVDT (Linear Voltage Differential Transducer) sensors are used to monitor the displacement of the lower planes of both tungsten plates. They have a measurement amplitude of 5 mm, are extremely accurate (relative accuracy given to be less than 0.5 %) and thus provide a very good estimate of the change in height of the pellet during the tests. Tests were all carried out at a pellet temperature of 1500°C ± 20°C at two different crosshead speeds of respectively 20 μm and 50 μm per minute. Assuming tests are uniaxial, the linear strain rates are estimated at 2×10^{-5} s^{-1} and 5×10^{-5} s^{-1}. Table 1 lists the conditions the various tests were carried out under.

2.3. Oxygen partial pressure control

The oxygen partial pressure is controlled by setting up a buffering reaction in the gas phase and equilibrating the material with it. A mixture of argon,

hydrogen and water vapour is used. The humidity level, hence oxygen pressure, is controlled by injecting into the carrier gas small and controlled quantities of oxygen upstream from the sample. This is done with a solid electrolyte (zirconia) oxygen pump [10, 19] and the oxygen partial pressures, dew points and total gas pressures are monitored both upstream and downstream from the furnace.

One must bear in mind though, that the range of oxidising conditions is necessarily limited as a result of using a given gas phase equilibrium (oxygen, hydrogen and water vapour in our case). This range is constrained towards the lower (reducing) and higher (oxidising) oxygen partial pressure values. In practice, the proportion of hydrogen used in the carrier gas determines the lowest achievable oxygen partial pressure values. Indeed, for such a gas mixture to act as an adequate buffer, a rule of thumb requires that both majority gas sepcies (H_2 and H_2O in this case) be present in proportions in excess of 10^{-3}atm. At a given temperature, the oxygen partial pressure of the gas phase is then proportional to the quantity $(p_{H2O}/p_{H2})^2$, where p_{H2O} and p_{H2} are the water vapour and hydrogen partial pressures respectively. The lowest achievable oxygen partial pressure is therefore obtained for the minimal value of p_{H2O} ($\approx 10^{-3}$atm.) and the maximal value of p_{H2}, $i.e.$ the maximum hydrogen content of the carrier gas mixture. A numerical application shows that at 1500°C, and for a 5% H_2 gas mixture, the lowest achievable oxygen partial pressure is roughly 3×10^{-13} atm. The upper limit is determined by the fact that tungsten readily oxidises so in practice, this precludes carrying out experiments at oxygen partial pressures in excess of 3×10^{-10} atm. (at 1500°C).

Prior to the high temperature compression test, we checked that the oxygen partial pressures at equilibrium upstream and downstream from the furnace were equal, and that these values were within 5% (relative) of the theoretical values.These checks are a demonstration that the gas phase is acting as a buffer throughout the system and that the sample is indeed subjected to the desired oxygen partial pressure. An important point to note is that the time scale over which equilibration occurs is long (in excess of 12 hours). This timescale is determined by the flow rate (12 l/h) used in relation to the furnace free volume (roughly 60 l).

3. Constitutive model and experiment modelling

In this section, we present the model representation of the compression experiments assuming either uniaxial or axisymmetric hypotheses. The latter assumption enables us to address the issue of an inhomogeneous distribution of strains in the pellet as a result of friction at the interface between the pellets and tungsten plates. The mtest [23] and licos [22] softwares are used depending upon whether a one or two-dimensional hypothesis is assumed. However, the material behaviour law is implemented independently of the representation through the use of the mfront code generator [23]. This tool has been coupled to a number of different finite element solvers including Cast3M which we used in this study. It has the advantage of enabling complex behaviour laws to be

5

implemented in a form which is straightforward and close to their mathematical formulation.

3.1. Constitutive model

Several types of models are used including a kinematic hardening law to represent the macroscopic viscoplastic behaviour of sintered uranium oxide. In contrast to a Norton type formulation, an internal stress variable is introduced which describes the material's transient hardening at the start of the test when dislocations multiply and prior to creep reaching a steady state[20, 12]. The corresponding constitutive equations may be expressed as follows:

$$\underset{\sim}{\epsilon}^t = \underset{\sim}{\epsilon}^e + \underset{\sim}{\epsilon}^{vp} \tag{1}$$

$$\dot{\underset{\sim}{\epsilon}}^{vp} = \dot{\nu}.\underset{\sim}{n} \tag{2}$$

$$\underset{\sim}{n} = \frac{\partial f}{\partial \underset{\sim}{\sigma}} \ with \ f = J_2(\underset{\sim}{\sigma} - \underset{\sim}{X}) \tag{3}$$

$$\dot{\nu} = \left(\frac{|J_2(\underset{\sim}{\sigma} - \underset{\sim}{X})|}{K} \right)^n \tag{4}$$

$$\dot{\underset{\sim}{X}} = \frac{2}{3} C \underset{\sim}{\epsilon}^{vp} - D \underset{\sim}{X} \dot{\nu} \tag{5}$$

In these expressions, $\underset{\sim}{\epsilon}$ designates either the total ($\underset{\sim}{\epsilon}^t$), elastic ($\underset{\sim}{\epsilon}^e$) or viscoplastic ($\underset{\sim}{\epsilon}^{vp}$) strain tensors. Equation (1) expresses the partition of the total strain tensor between elastic and viscoplastic components. Equations (2) and (3) are known as the normality rule and express the fact that the plastic deformation flows normal to the surface defined by a constant value of function f. In equation (3), J_2 represents the second deviatoric stress invariant, $\underset{\sim}{X}$ represents the internal stress variable and in equation (4), $\dot{\nu}$ is the equivalent visco-plastic strain rate. The model in effect has four parameters (K, C, D and n). K and C are homogeneous to stress, whilst D and n have no dimensions.

The formalism we have adopted is that of large transformations and within this approximation, the logarithmic strain formalism is adopted here [31]. In addition to constituting a means of describing the large strain fields encountered in our experiments, it has the advantage of conserving a number of features characteristic of the more standard small strain formalism amongst which the fact that the trace of a strain tensor is zero for a constant volume deformation process.

3.2. Uniaxial modelling and data analysis

In this section we describe a uniaxial representation of our experiments and define what data one should analyse in order to identify a constitutive model. Experimentally, the pellet is free of mechanical load and heated to the temperature at which the experiment is carried out. After an appropriate equilibration time, a load is applied by imposing a constant cross-head speed. The *in situ* displacement sensors provide a measure of the change in the height of the pellet.

In the large strain formalism, we seek to define the appropriate deformation gradient tensor which is the differential of the vector function which transforms the solid from its reference state to its deformed state. One may write:

$$\vec{r} = \vec{R} + \vec{u}(\vec{R}) \tag{6}$$

In the above relationship, $\vec{r}(x,y,z)$ and $\vec{R}(X,Y,Z)$ designate the particle coordinates in the deformed and reference configurations respectively and $\vec{u}$ is the displacement map. Differentiating with respect to $\vec{R}$ yields the following expression for the deformation gradient tensor $\underset{\sim}{F}$:

$$\underset{\sim}{F} = \underset{\sim}{Id} + \underset{\sim}{d}u(\vec{R}) \tag{7}$$

where $\underset{\sim}{Id}$ is the identity tensor. In a uniaxial representation of the problem, all non-diagonal terms of the deformation gradient tensor are nil, the meaningful term being the axial component which, assuming the axial strain is uniform during the experiment, may be written as:

$$F_{zz} = 1 + \frac{\partial u_z}{\partial Z} = \frac{h^h(t) - h^h(0)}{h^c(0)} + f(T) = \frac{\Delta h^h(t)}{h^c(0)} + f(T) \tag{8}$$

In this relationship, u_z represents the axial component of $\vec{u}$; $h^h(t)$, $h^h(0)$ and $h^c(0)$ designate the height of the pellet at time t as measured during the experiment (the superscript refers to the high temperature value), at the beginning of the high temperature part of the experiment and at room temperature respectively; $f(T)$ is related to the temperature (T) dependent thermal expansion coefficient of the supposedly homogeneous material. This relationship shows that in a near constant cross-head speed experiment, the pellet loading to consider at time t is that given by the difference between the two displacement values provided by the displacement sensors described in section 2.2.

We now determine which experimental data the model representation should be assessed against. Throughout the experiments, the load L_z exerted on the pellet through the column of the compression machine is monitored. To determine its calculated counterpart, one expresses the fact that creep induces a deformation at constant volume (see equations (2) and (3)). As a result, the product of the pellet surface and pellet height is assumed constant during the viscoplastic deformation. It follows that the calculated load is given by:

$$L_z^{calc.}(t) = \mid \sigma_z^{calc.} \mid S(t) \approx \mid \sigma_z^{calc.} \mid \frac{S(0)h^h(0)}{h^h(t)} \tag{9}$$

where $\mid \sigma_z^{calc.} \mid$ is the absolute value of the calculated axial component of stress (equal under the uniaxial hypothesis to the Von Mises stress $\sigma^{vm.}$) and $S(t)$ is the surface area of the pellet at time t. An estimate of $S(0)h^h(0)$ is used to

7

derive $L_z^{calc.}(t)$ based on our knowledge of the thermal expansion coefficient of UO_2.

The methodology for identifying a viscoplastic model consists therefore in imposing the displacement through equation (8) and minimising the difference between the calculated (expression (9)) and experimental loads. As is discussed in section 4, a given experiment enables parameters C, D and either K or n to be determined unequivocally.

3.3. Two dimensional modelling and data analysis

We have also developed a two dimensional axisymmetric model which represents the pellet as a perfect cylinder. The supposed symmetry of the problem requires only half the pellet be modelled. The nodes along the pellet upper plane are subject to an axial displacement given by the measured changes in the pellet height during the viscoplastic deformation stage of the experiment. The load is calculated by integrating the axial component of stress along the top plane of the sample. The quantity obtained may then be compared to its measured counterpart. To summarise, the input data file and the material behaviour laws in our uniaxial and two dimensional representations are identical.

We report only two extreme cases: perfect slip or clamping between the pellet and tungsten plates. An eight node quadratic, axisymmetric element is used in the modelling and the pellets which have a height and radius of approximately 16 mm and 8 mm respectively are modelled with 20 elements in the radial direction and 45 elements in the axial direction.

4. Results: model validation and data analyses, microstructural characterisations

In section 4.1, we first use experiment number 1 from table 1 ($p_{O2} \approx 1.3 \times 10^{-12}$ and $\dot{\epsilon} \approx 2 \times 10^{-5}\text{s}^{-1}$) to better understand the macroscopic phenomena and reveal the different creep stages that are occurring during our experiments. We thus get a preliminary feel for the validity of the uniaxial hypothesis and potential caveats. Section 4.2 is devoted to an analysis of experiment number 1 with the one and two dimensional descriptions outlined in section 3.1. This helps us to quantify two-dimensional effects. Finally an analysis of the entire set of macroscopic data is proposed in section 4.3. Section 4.4 is concerned with EBSD observations of samples tested under different oxygen partial pressures.

4.1. Analysis of experimental data from test number 1

Assuming the deformation process occurs at constant volume, equation (9) may be inverted to express the experimentally determined Von Mises stress under uniaxial hypotheses. Figure 1 shows the stress curve under these assumptions along with the the change in length of the pellet during the high temperature compression sequence, derived as the difference between the two extensometer signals. Note that by convention positive $h(t)$ values indicate a reduction in pellet length.
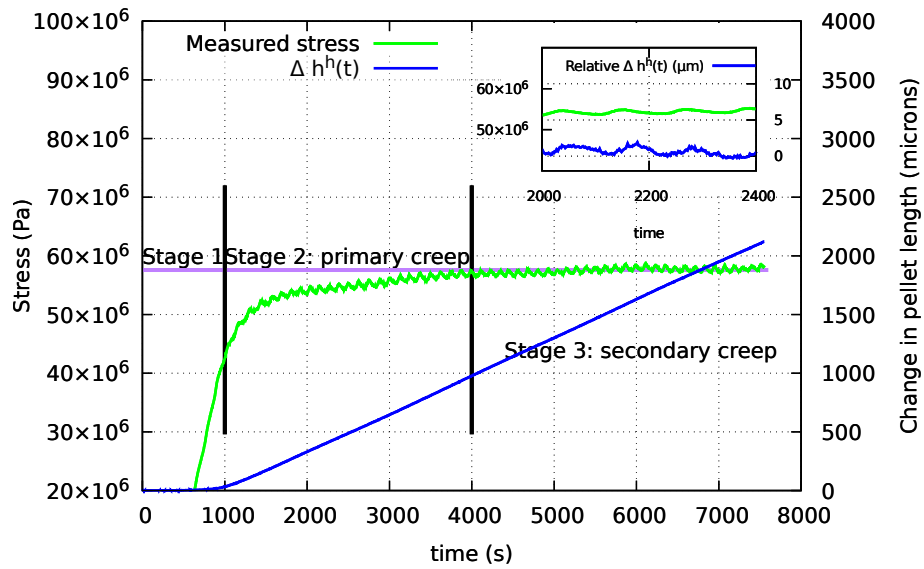
Several comments may be formulated:

Figure 1: Left–hand vertical scale: uniaxial, experimental Von Mises stress for experiment 1 assuming a constant volume deformation process (purple curve). Right–hand scale: change in pellet length (blue line). The inset represents both stress (green line reported on the left–hand scale) and the relative change in pellet height (blue line on the right–hand side vertical axis); by which we mean the change in pellet height corrected for the decrease, proportional to time, induced by the movement of the crosshead at a constant speed of *circa*. 20 μm/min. The expansion along the x and y axes reveals small pellet height fluctuations of 1 to 2 μm. This demonstrates that pellet height fluctuations occur and that they correlate to stress fluctuations.

- The stress curve broadly follows the usual trend involving an initial hardening of the material (primary creep) followed by a period during which stress attains a quasi steady-state (secondary creep).

- Stress is subject to oscillations that become visible after approximately 1000 seconds into the experiment. The inset in Figure 1 is an expansion over 400 seconds of changes in stress (left–hand side axis) and of the relative changes in pellet height (right–hand side axis). By this we mean pellet height corrected for the linear decrease at a constant rate of 20 μm/min imposed by the crosshead movement. The inset demonstrates two things. First, that the pellet is subjected to small but measurable fluctuations of strain, in addition to the overall pellet contraction along the vertical axis due to the crosshead movement. Second, that these fluctuations are correlated to the observed stress fluctuations. We have since demonstrated that these periodic changes are due to temperature fluctuations of the water used to cool the device down. We surmise that these are sufficient to induce a contraction or expansion of the entire setup, inducing small but detectable additional strains upon the pellet. At this stage, we can only conjecture that the strain fluctuations are the cause of the stress fluctuations.

- At the start of the experiment, the pellet length hardly changes as backlash in the system is recovered. However, roughly 1000 seconds into the experiment, the change in pellet height follows the crosshead displacement closely.

This preliminary analysis of macroscopic results indicates that a constant crosshead speed experiment comprises three, possibly overlapping, stages. The first is due to the backlash of the mechanical setup. During this initial stage, the Cauchy stress, increases sharply with no noticeable effect upon the pellet height but as the period draws to a close, primary creep sets in as a result of the material beginning to be loaded in earnest. During the second stage, primary creep occurs and is picked up as hardening on the stress curve. Finally, stress values level off and steady state or secondary creep begins. During this period, the load curve (not represented) continues to increase practically linearly but this increase is compensated through equation 9 by an increase in the pellet diameter, so that on balance the axial stress remains quasi–constant.

4.2. One and two dimensional modelling of test number 1

In order to ascertain the qualitative conclusions from the preceding section, we now apply the uniaxial and axisymmetric models outlined in section 3. We choose to fix a number of parameters before seeking to identify an optimal set. For instance, the stress exponent in equation (4) is set to 4, which is in the range of values reported for polycristalline ceramics[11] and UO_2 [37] in particular. Such a high stress exponent value (greater than 3) is characteristic of dislocation creep [32] which is expected at temperatures and strain rates relevant to this study.

10

The value of K is key to reproducing the steady-state flow stress through equation (4), whilst C and D control the rapid changes in stress corresponding to the primary creep stage. Figure 2 shows the result of our model cal-
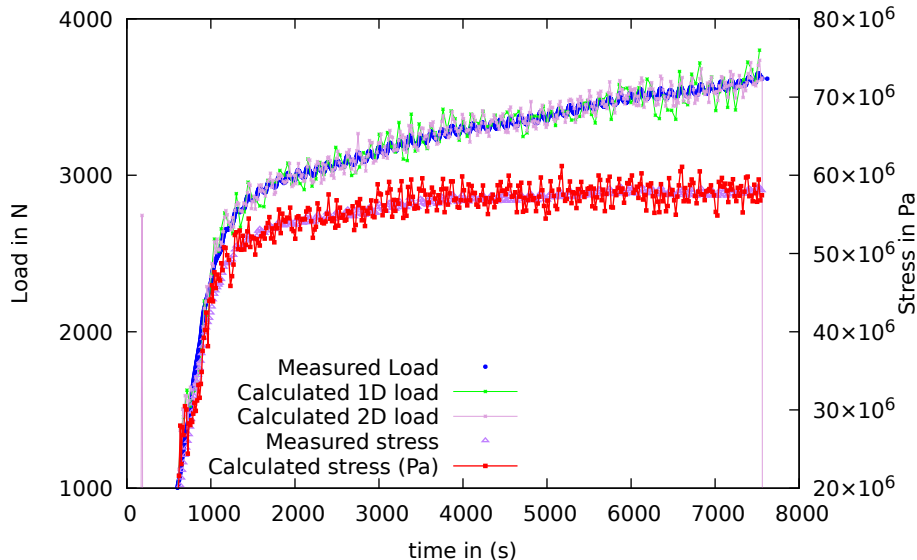

Figure 2: Comparison of *in situ* experimental data and model calculations assuming experiment 1 is uniaxial in nature. The 2D calculation is performed assuming frictionless glide between the tungsten plates and the fuel pellet.

culations in comparison to the *in situ* macroscopic experimental data. The numerical parameters chosen for this analysis are as follows: $\{K, C, D, n\} = \{790 \times 10^6 \text{ Pa}, 300 \times 10^6 \text{ Pa}, 45, 4\}$. The figure illustrates rather emphatically that the model (material model and geometrical representation) is capable of reproducing the experimental data well and attention must further be drawn to the fact that the oscillations that appear in the stress or load are also quite well described. This is a confirmation of the fact that they are caused by an experimental caveat that induces an additional strain on the pellets contained in the pellet height data provided by LVDTs (as illustrated in Figure 1 and which we use as input for our stress calculations). One can also note that the 2D axisymetric calculation assuming no friction between the tungsten plates and the sample faithfully reproduces the uniaxial approach.

However, it is well known[35] that the right cylinder shaped samples take on a barrel shape following a compression test. In order to get a feel for the level of friction there is between the tungsten plates and the samples, we report two additional axisymetric calculation assuming the plates and uranium dioxide specimens are clamped. An analysis of the *in situ* macroscopic data shows that changing parameter K (760×10^6 Pa) slightly, suffices to reproduce the data with the same level of consistency as shown in Figure 2. In addition, it is now

possible to compare the calculated pellet profile assuming infinite friction to the corresponding experimental data. This comparison is shown in Figure 3. The experimental data are obtained from a laser measurement of the pellet diameter along the length of the pellet height. Four generating lines are thus characterised and average values are represented in Figure 3.
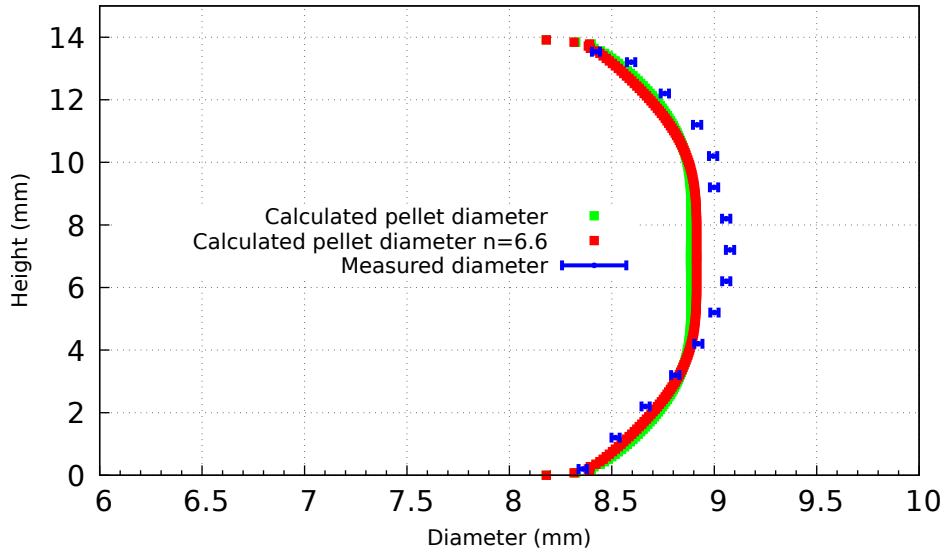

Figure 3: Comparison of the pellet diameter averaged over four generating lines with a 2D model calculation assuming the pellet is clamped between the two tungsten plates. Two calculations are presented with different values of n and K. The green data points are obtained for n and K values of 4 and 790 MPa., whereas the red data points where obtained for values of 6.7 and 271 MPa.

The calculated profile reproduces the experimental data quite well. A comparison between experimental and calculated diameters at the top and bottom of the pellet and the general shape of the pellet following the test, would seem to indicate that the contact conditions are probably closer to infinite friction than they are of no friction, although the former hypothesis does not quite capture the entire pellet profile.

Finally, we have included in Figure 3 a calculation carried out for different values of n and K (6.7 and 271 MPa respectively). Results with these latter parameters entail no loss of quality. This illustrates the fact that K and n are related parameters and that it is impossible to determine their value from a single experiment.

4.3. Analysis of all remaining experiments

In choosing a relatively high pellet height to diameter ratio, it was our intention to mitigate multidimensional effects induced by friction at the interface between the tungsten plates and the samples. The preliminary analyses of our

data (section 4.1) and the fact that taking into account friction forces in a two-dimensional axisymmetric modelling approach does not fundamentally modify the level of axial stress the pellet is subjected to (section 4.2), both suggest that our experiments are essentially uniaxial. Further, in our systematic analysis of the experiments carried out using the Frederick and Armstrong model (see [20] and section 3.1), we verified the fact that the axial component of the internal stress tensor was always small (less than 10 %) in comparison to the Cauchy stress of the sample. As a result, the experimental data were analysed using the following phenomenological steady state creep law for non stoichiometric oxides[6, 5, 8, 32]:

$$\dot{\nu} = A p_{O_2}^{\alpha} \frac{\sigma_{vm}^n}{k_b T} e^{\frac{-E_a}{k_b T}} \tag{10}$$

Equation (10) is obviously derived from equation (4) in which σ_{vm} is the Von Mises stress, *i.e.* $|J_2(\underline{\sigma})|$, n and α are the stress and oxygen partial pressure exponents, E_a an activation energy. What is presented as a proportionality constant in this equation is in fact a weakly varying function of temperature, especially as a result of its dependence upon the elastic constants of the material. A also covers the influence of the microstrucre. Several phenomenological creep laws have been proposed in which A is a power law of the grain size, the increase of which has a tendency to soften the material in the dislocation creep regime [38, 7].

The values of steady state flow stress (Von Mises) were determined for each of the experiments reported in Table 1 and plotted in Figure 4 as a function of oxygen partial pressure.

Several comments may be made in relation to Figure 4. Firstly, both sets of data points appear aligned in this log-log representation and the slopes of both lines are similar within the experimental scatter, roughly equal to 0.04. Note also that in view of the assumed steady state formulation corresponding to equation (10), these slopes represent the ratio of the exponent of the oxygen partial pressure to the exponent of stress (*i.e.* $\frac{\alpha}{n}$ in equation (10)).

Based on these results, one may also estimate tentative values of the stress and oxygen partial pressure exponents. In order to do so one may raise to the power $\frac{1}{n}$ and take the logarithm of both sides of equation (10):

$$log_{10}(\dot{\nu}) = B(T) + n \times log_{10}(p_{O_2}^{\frac{\alpha}{n}} \sigma_{vm}) \tag{11}$$

In this expression B is assumed to be a function of temperature only and if $\frac{\alpha}{n}$ is considered to be a constant characteristic of the material response and independent of temperature, then one can expect the experimental data points (*i.e.* $(log_{10}(\dot{\nu}), log_{10}(p_{O_2}^{\frac{\alpha}{n}} \sigma_{vm}))$ couples) to define a line, the slope of which provides an estimate of n. In order that the mechanical variables on either side of equation (11) be consistent, we optimized the model parameters of equation (10) for all experiments. As a result, the values of $\dot{\nu}$ we consider as experimental represent the finite logarithmic strain rate as outlined in section 3.1.

Figure 5 shows a plot of the strain rate for the different experiments carried out as a function of the variable $(p_{O_2}^{\frac{\alpha}{n}} \sigma_{vm})$ for a reasonable value of $\frac{\alpha}{n}$ of 0.04.
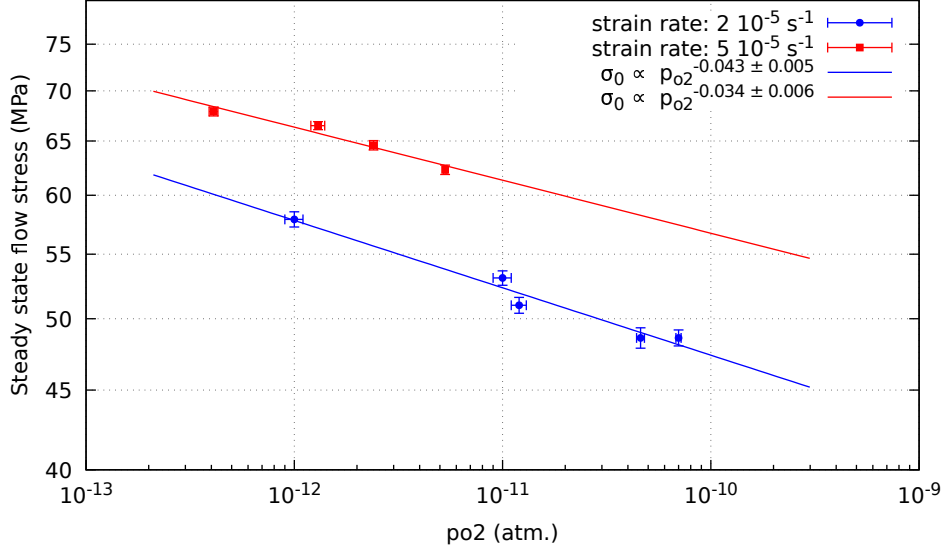
13

Figure 4: Steady state flow stress as a function of oxygen partial pressure for tests carried out at $1500°C$ and at approximate strain rates of 2×10^{-5} s^{-1} and 5×10^{-5} s^{-1}.

Under these conditions, the stress exponent is equal to roughly 6.7, whence α works out at $\approx \frac{1}{3.7}$. Although the lack of data points precludes a meaningful satistical analysis, the $\frac{\alpha}{n}$ quantity may be estimated between roughly 0.028 and 0.048, parameters which correspond to (n, α) couples equal respectively to $(5.6, \frac{1}{6.4})$ and $(7.3, \frac{1}{2.8})$.

4.4. Microstructural characterization of creep tested samples

Several pellets were characterised prior to and following the creep experiments using EBSD. The pellets that were earmarked for this had identical microstructures prior to testing and were cut along the compression axis and ground and polished following procedures outlined in previous reports[3, 4]. The microstructures of three samples were characterised using scanning electron microscopy and EBSD. All three samples (referenced subsequently as sample 1 from reference [4], sample 2 and sample 3, see section 5.3) were creep tested at identical strain rates as samples from tests 1 through 5 indicated in Table 1. The total linear strains reached were respectively 12%, 13.3% and 13.8% for samples 1, 2 and 3.

The main difference between the three samples lies in the oxygen partial pressure they were mechanically tested under. The oxygen pressure relative to sample 1 was not monitored but is considered to be the lowest achievable oxygen pressure as the corresponding test was carried out in a dry argon–hydrogen mixture. Samples 2 and 3 correspond to tests 1 and 4 in Table 1. Large scale SEM images were taken of all three pellet sections whence it was observed that
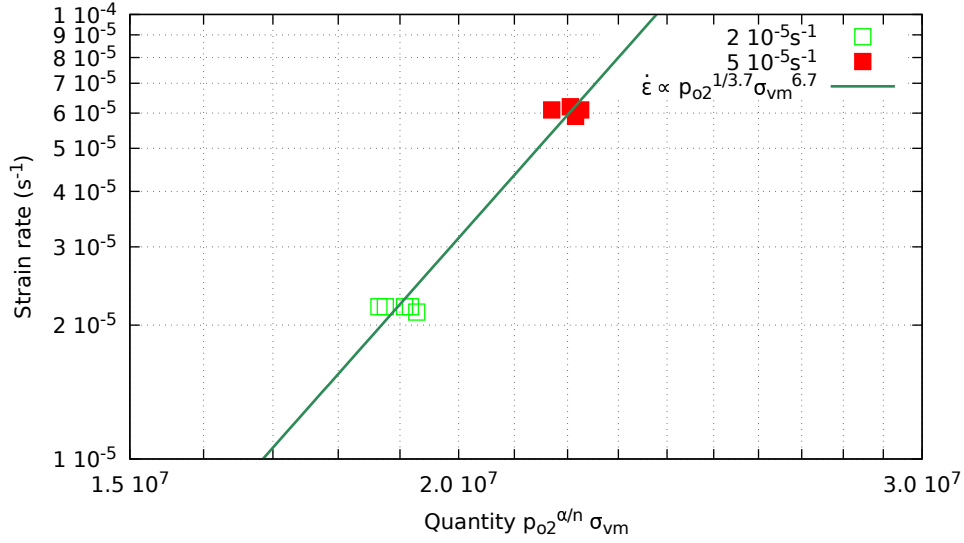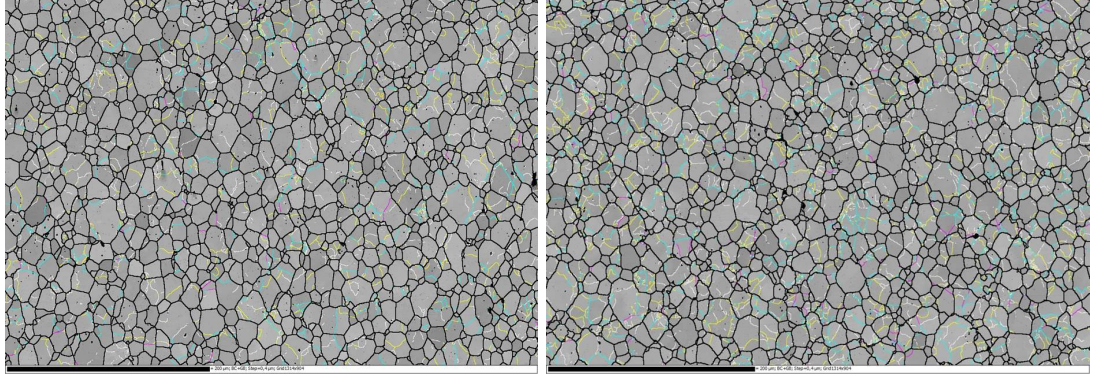
14

Figure 5: Estimate of the stress exponent relative to equation (10) with data points plotted assuming a value of $\frac{\alpha}{n}$ of 0.04; under these conditions, α is estimated at $\approx \frac{1}{3.7}$.

the two pellets tested at the highest oxygen partial pressures presented regions in which a much greater than average porosity was present. It was noteworthy that some of these regions lay away from the mid-pellet plane. Sites were therefore chosen in which EBSD characterizations were carried out. The EBSD mapping conditions have been outlined elsewhere[3]. Suffice it to say here that maps were acquired in 0.4 μm steps with the electron beam scanned over a 530×360 μm^2 area (corresponding to 1314×904 pixels). Conditions were optimised to detect small misorientations between adjacent regions of the crystal [34].

The EBSD characterization from four regions are shown in Figure 6: a region located in the mid–pellet plane from samples 1 and 2 (Figures 6a and 6b) and a region from samples 2 and 3 in which the SEM examinations revealed a greater void fraction than elsewhere at the surface of the section (Figures 6c and 6d). The voids or cracks that can be seen in these figures , are distinctly intergranular in nature. Such features are characteristic of the ultimate consequence of GBS (Grain Boundary Sliding) and have been reported previously in relation to this material[15].

The EBSD maps were used to identify the presence of sub–boundaries according to procedures described elsewhere[3, 34, 4] and involving appropriate filtering of the data and minimisation of misorientation noise. The images reveal networks of sub–boundaries that characterize the response of the material to plastic strain. These sub–boundaries are interfacial regions that separate areas of the original grain that have become slightly misoriented following the creep test. Misorientation angles above 5° have been shown to correspond es-

a) Sample 1 (see [3])tested at the lowest p_{O2}; central region of the pellet.

b) Sample 2: tested at $p_{O2} \approx 10^{-12}$ atm.; central region of the pellet.
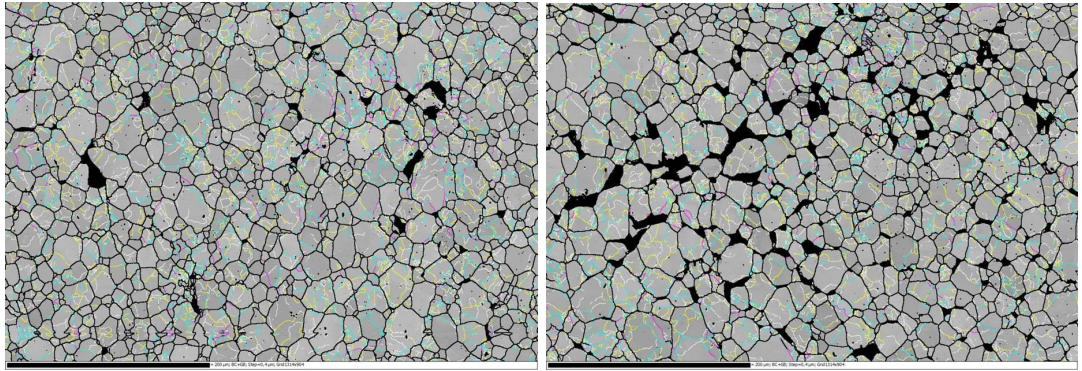
c) Sample 2: tested at $p_{O2} \approx 10^{-12}$ atm.; region of high void fraction.

d) Sample 3: tested at $p_{O2} \approx 5 \times 10^{-11}$; region of high void fraction.

Figure 6: $530 \times 360 \ \mu\mathrm{m}^2$ EBSD maps from different regions of the pellets. Colored lines represent low angle sub–boundaries. Misorientation angle: $[0.25, 0.5[$ (white); $[0.5, 1[$ (yellow); $[1, 3[$ (turquoise); $[3, 5[$ (pink); ≥ 5 (black). Non–indexed EBSD points are also drawn in black.
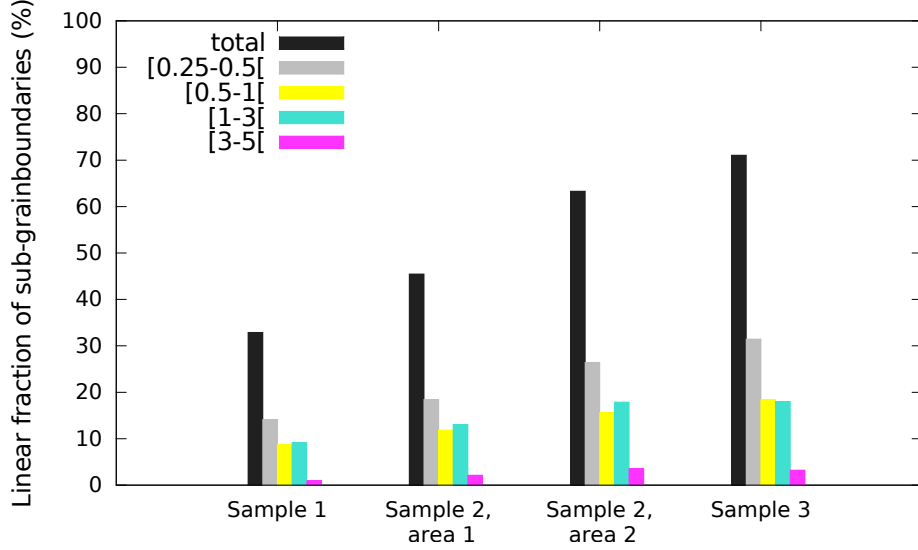
16

Figure 7: Set of histograms indicating the linear fraction of sub–boundaries for each of the EBSD maps indicated in Figure 6

sentially to grain boundaries originally present in the material. Figure 7 shows a histogram representation of the linear fraction of sub–boundaries for each of the areas corresponding to Figure 6. Sub–boundaries are apportioned in four classes of increasing misorientation between 0.25 ° and 5 °. Each sub–boundary class is represented according to the same colour coding as that used in Figure 6. The total fraction of low angle boundaries, shown as black bars in this figure, appears to increase substantially with increasing oxygen partial pressures.

5. Discussion

It has been widely reported in the literature, that the viscoplastic behaviour of UO_2 in the temperature range we are concerned with here, falls in either of two categories depending upon the level of stress the material is subjected to and the grain size [7, 38]. At lower stresses (typically less than 25 MPa for this material microstructure and at this temperature[3]), both the strain rate and the deformation mechanisms are thought to be related to some self–diffusion coefficient and the creep rate is roughly proportional to stress.

At higher stresses on the other hand, the stress exponent rises and so called power law creep kicks in. For similar strain rates to those we are dealing with here, widely varying values have been suggested for both single crystal and poly-crystalline materials: ranging between 4 and 5 (see [36] and reference therein), between 7 and 8 at 1500°C [15], between 5 and 9.2 at 1460°C depending upon grain size[38](7.4 for materials with a grain size of 11 μm), 6.8 at 1500°C [13],

17

7.2 at 1500°C for materials with identical microstructures to ours[3].

We now attempt to identify the creep mechanisms involved in our experiments by combining results available in the literature, an analysis of the exponents estimated from our experiments (sections 5.1 and 5.2) and an interpretation of the microstructures observed and the effect of the oxygen pressure thereon (section 5.3).

5.1. Stress exponent

It is noteworthy that in Colin's work [13], several so called dip test experiments were carried out at 1350°C and at relatively high stress levels (*circa* 75 MPa) which revealed a behaviour of UO_2 typical of recovery creep. Philibert [32] derives a phenomenological expression for the steady state recovery creep rate based on the Orowan equation and suggests that in practice, one of the two criteria for ascertaining whether one is dealing with recovery creep is the fact that the stress exponent is greater than, or equal to, three. This is generally the case for UO_2 including in the work carried out in this investigation.

We have seen in the introductory comments to this section how close the stress exponent values at 1500°C alluded to in the more recent studies are to ours (6.7, see section 4.3). This suggests that similar creep mechanisms are at work in all of these studies.

However, the consistency between studies does not in itself justify the actual value of the stress exponent and indeed Poirier([33], p. 111) appears to doubt whether stress exponent values in excess of 5 actually reflect true power law creep. Values of stress exponents have been reported to range between 6.8 and 11.5 in NiO [8] and between 6.3 and 8.5 in CoO[17] depending upon temperature, possibly suggesting power law breakdown. Weertman[39] first suggested a creep model for pure metals, based on microstructural considerations, that predicts a stress exponent of 4.5 in which climb constituted the recovery process and consequently bulk self-diffusion, was the rate controlling processes. He subsequently made more complex assumptions which lead him to suggest exponents of 5[41] and even 6[40]. Regarding the former, he assumed the presence of screw and edge segments whose annihilation occurs not through climb but through cross–slip, as observed in aluminium by Caillard and Martin[9]. Ultimately though, in all of Weertman's approaches, the rate controlling mechanism remains climb of dislocations hence self-diffusion. It is also probably worth mentioning that in metals, discrete dislocation dynamics models have been developed with the aim of describing both dislocation and diffusional creep[25]. Although self-diffusion is the only recovery process taken into account, these authors' model predicts stress exponents at high stresses ranging between 5 and 7. Whether climb is the only recovery process or whether it can operate in conjunction with cross slip to determine the strain rate as suggested by Poirier ([33], p. 114) remains a matter of debate in general, and for uranium dioxide in particular.

The literature and arguments we have discussed in this section assume the existence of a single sub-lattice. In the next section we see how the existence of two sublattices affects these considerations and discuss the central role the

oxygen partial pressure dependence plays in ascertaining the influence of self-diffusion in visco-plastic deformation processes in UO_2.

5.2. Oxygen partial pressure exponent

In non-stoichiometric binary oxides, at a given temperature and pressure, the oxygen partial pressure controls point defect concentrations. As a result, determining the creep rate as a function of oxygen pressure is liable to indicate which defects are influencing this property and how. Philibert[32] shows that if diffusion controlled climb is at the heart of the recovery processes, then it is lowest defect diffusion coefficient that determines the climb velocity, hence creep rate. This has been demonstrated in NiO[8] and CoO[17] which are cation deficient oxides and in which oxygen is, as a general rule, the slowest of the two migrating species

Seltzer and co-workers[37] report a strong effect of non–stoichiometry upon strain rate in the dislocation creep regime of UO_2 single crystals. Unfortunately, results are provided in terms of composition dependence, which is not an intensive thermodynamic quantity appropriate for expressing material behaviour laws. The point in this study though is that the steady state strain rate is an increasing function of oxygen content hence oxygen pressure. Uranium dioxide is essentially an oxygen excess oxide in which uranium self-diffusion lies several orders of magnitude below oxygen self-diffusion. Uranium self-diffusion is thought to occur via a vacancy mechanism [30, 18] and so the uranium self-diffusion dependence upon oxygen partial pressure should also mirror the dependence upon this quantity of the uranium vacancy concentration. Although precise values of deviation from stoichiometry are fraught with uncertainties very close to stoichiometry, the analysis of chemical potential of oxygen data carried out by Baichi [2] (p.45, Fig. 20) and co-workers but originally obtained by Wheeler and Jones [42] and Markin and Bones [29] would suggest that at 1500°C, and in the oxygen partial pressure range studied in this work, the deviation from stoichiometry of our material is of the order of 10^{-3} or less. Under those circumstances, one expects oxygen defects to be present as isolated interstitials and an essentially purely ionic behaviour of UO_2 to prevail[21] in which uranium vacancies bear a -4 charge state. We make the following assumptions:

- Defect populations (in Kröger Vink notation) are (in order of abundance): h° (holes or U^{5+} ions), $O_i^{''}$ (doubly charged oxygen interstitials), $V_U^{''''}$ (-4 charged uranium vacancies), $V_O^{\circ\circ}$ (doubly charged oxygen vacancies).

- the main defect equilibria are as follows: $\frac{1}{2}O_2 \rightleftharpoons O_i^{''} + 2h^\circ$ (oxidation equilibrium), $O_i^{''} + V_O^{\circ\circ} \rightleftharpoons \varnothing$ (oxygen Frenkel equilibrium), $V_U^{''''} + 2V_O^{\circ\circ} \rightleftharpoons \varnothing$ (Schottky equilibrium).

- electro–neutrality is expressed as: $[h^\circ] \approx 2[O_i^{''}]$.

Assuming thermodynamic equilibrium, the three temperature dependent defect equilibria above may each be expressed in terms of a mass–action law to

19

provide the relationship between equilibrium constants and defect concentrations [26]. The electroneutrality condition ($[h^\circ] \approx 2 \times [O_i^{''}]$) provides a fourth equation which makes it possible to determine all four unknowns (*i.e.* $[h^\circ]$, $[O_i^{''}]$, $[V_O^{\circ\circ}]$ and $[V_U^{''''}]$) as a function of oxygen partial pressure at a given temperature. One thus shows that the uranium vacancy concentration should follow a power law of the oxygen partial pressure with an exponent of $\frac{1}{3}$ and is therefore an increasing function of oxygen pressure. Assuming a vacancy mediated uranium diffusion mechanism, the self-diffusion coefficient of uranium is given by: $D_U = f_U[V_U^{''''}]D_{V_U}^{\circ} e^{\frac{-E_m^{V_U}}{k_b T}}$ (with f_U the correlation factor for a vacancy mechanism in a face centered cubic crystal, E_m the uranium vacancy migration barrier and $D_{V_U}^{\circ}$ the pre–exponential factor of the uranium vacancy diffusion coefficient coefficient), one can rewrite equation (10) as:

$$\dot{\nu} = A(T)p_{O_2}^{\frac{1}{3}}\sigma_{vm}^n e^{\frac{-E_m}{k_b T}} \tag{12}$$

The sign and range of values of α derived in our experiments (section 4.3) are compatible with this expression and associated hypotheses, *i.e.* that uranium self-diffusion is the rate limiting phenomenon.

5.3. Creep tested microstructures

The second criterion that Philibert[32] suggests can be used as evidence of recovery creep is a characteristic microstructure involving the formation of subgrains with well defined sub-boundaries. This is exactly what may be inferred from the EBSD characterizations presented in section 4.4. In fact, this fragmentation or subdivision of original grains induced by the formation of low angle sub-boundaries has been observed by several authors in relation to polycrystalline UO_2 creep tested under similar conditions to ours[15, 34, 4]. The actual sub-boundaries have also long been associated from Transmission Electron Microscopy (TEM)[1, 15] and more recently Electron Channeling Contrast Imaging (ECCI)[3, 28] examinations, with the rearrangement of dislocations which form cells of specific geometry. Cell structures such as hexagons for example have been shown to result from interacting screw dislocations belonging to the primary slip systems of UO_2, *i.e.* $\{100\} < 110 >$ through some cross-slip mechanism involving $\{111\}$ planes[1, 15, 3]. A wide variety of other geometrical arrangements has been observed, some involving the $\{110\} < 110 >$ slip system[1]; Ben Saada, Mansour and co-workers[3, 28] insist upon the variety of situations that may be encountered in a single polycrystalline specimen.

Figure 7 shows the linear fraction of sub–boundaries to be substantially lower for sample 1 than for sample 2. The single differentiating feature between the two specimens, which belong to the same manufacturing batch, is the oxygen partial pressure they were creep tested under (*i.e.* identical creep rates and very similar final strains). Sample 1 was tested under Ar–5% H_2 so was exposed to the lowest possible oxygen potential. Although the value itself was not recorded, we know it must have been two to three orders of magnitude below the corresponding value for sample 2. Samples 2 and 3 were tested at 1.3×10^{-12}

and 4.8×10^{-11} atm. respectively and correspond to tests 1 and 5 in Table 1. Again, the linear fraction of low angle sub–boundaries appears to be greater in the region characterised from sample 3 than in an equivalent region of sample 2. One could argue that the suggested correlation between linear fraction of low–angle boundaries and oxygen partial pressure be subject to the caveat that this intensive thermodynamic quantity enhances grain growth. A cursory check of the data relating to Figures 6a and 6b based on the intercept method, suggests very little difference in grain size, if any. It was more difficult in regard to sample 3 to check for signs of grain growth following the test on account of the microstructure. More systematic investigations would be required, involving E.B.S.D. characterisations over wider areas, in order to conclude definitively as to whether the greater linear fraction of low angle boundaries observed at higher oxygen potentials reflects the effect of creep alone.

However, the other feature that stands out from microstructural characterizations detailed in section 4.4 (see Figures 6c and 6d) is the emergence in the pellet bulk, of pockets with a high void fraction. No such observations were made for sample 1 tested at low oxygen partial pressure and we have observed that the volume fraction of the pellet that is concerned by these features appears to increase with increasing oxygen pressure. This suggests that at roughly 13% strain, and under oxygen pressures consistent with those of sample 2, a third stage of creep has set in. One would expect the volume fraction of these areas to increase if the test were pursued and that this would lead to an irreversible damage of the sample.

Assuming the microstructures we have characterised are representative of a quasi steady–state, one may wonder why samples of identical initial microstructure tested at identical strain rates and similar final strains should show such differences. This observation illustrates the role of oxygen pressure as an intensive thermodynamic quantity: just as the steady–state creep law must depend upon the oxygen partial pressure so does the material microstructure, of which, the linear fraction of sub–boundaries presumeably and the high void fraction regions, are characteristics.

Several analytical expressions have been proposed for GBS induced viscoplastic deformation in metals. In Langdon's model[27] in which dislocations move through glide and climb along regions contiguous to the grain boundary, the strain rate is proportional to the product between the square of the external stress and the bulk diffusion coefficient; this latter property is therefore a factor common to both GBS and dislocation creep.One may anticipate two consequences. Firstly, during steady state creep, dislocation creep will dominate but as GBS proceeds, wedge type microcracks are liable to form at the interface between two grains or at triple junctions and propagate along the length of the grain boundary[43]. Secondly, the kinetics of intergranular decohesion should follow the same oxygen partial pressure dependence as the cation self-diffusion coefficient so that the analysis of section 5.2 still holds. Intergranular decohesion signals the beginning of the last stage of the deformation process.

On–going work is focusing on more systematic investigations of the effects of strain rate, oxygen partial pressure and temperature in order to build upon

the current findings. In particular, in this present study, we have looked at composition regions in which the behaviour of our material remains essentially ionic. Regions of more oxidising partial pressures should be investigated[24]. Further, more complex relaxation experiments are being undertaken so that a macroscopic recovery creep model may be identified. These additional tests aimed at deriving a viscoplastic model of more general applicability must also involve bending tests which induce more complex, non–uniform loading conditions. Additional microstructural examinations of the samples are required in order to confirm the deformation mechanisms and determine changes in key microstructural features (cell sizes, geometrically necessary dislocations, dislocation spacing...).

Such systematic and fundamental sets of data could undoubtedly provide a solid foundation on which to build discrete and continuum dislocation dynamics models or even develop phase field approaches capable of predicting dislocation pattering and incorporating diffusive or relaxation mechanisms[14]. They should also provide a means of estimating cation self-diffusion coefficients in actinide oxides for which there is an extreme dearth of data.

6. Conclusions

We have carried out compression experiments on dense polycrystalline uranium dioxide at $1500°C$ and two different strain-rates. At each strain–rate, the effects of the oxygen partial pressure were studied. The macroscopic experimental data consists of an in situ measurement of the change in pellet length, hence its linear strain, and of the load exerted via the column on the sample. One– and two– dimensional axi–symmetric models were developed to interpret the experiments with a kinematic hardening material behaviour law involving a single internal variable. The analyses were implemented using a finite logarithmic strain approach.

The analysis of the data in one and two dimensions shows that the experiments are essentially uniaxial vindicating the choice of pellet geometry. The strain rates are high enough to induce dislocation creep and both analytical and numerical analyses of the macroscopic experimental data show that the experiments are characterised by a two stage process involving primary and quasi steady–state creep.

We show that the steady state strain rate is reasonably well represented by a power law of stress and oxygen partial pressure with exponents of roughly 6.7 and $\frac{1}{3.7}$ respectively. The former exponent, is close to previously reported values for polycristalline uranium dioxide in these temperature and strain rate ranges. The latter exponent may be regarded as indicative of a recovery creep process in which climb is the underlying rate controlling mechanism. Our data are consistent with a strain rate controlled by vacancy mediated volume diffusion of cations, with vacancies in a -4 charge state.

A microstructural examination of a limited number of samples confirms we are dealing with recovery creep processes. The response of the material to stress at high temperature involves the formation of low angle boundaries within the

original material grains. This phenomenon appears to be more important in samples tested at higher oxygen partial pressures. In addition to grain subdivision, grain boundary sliding is observed.

[1] A. Alamo, J. Lefèbvre, and J. Soullard. Déformation plastique du bioxyde d'uranium : Observation des sous-structures de dislocations. *Journal of Nuclear Materials*, 75(1):145–153, 1978.

[2] M. Baichi, C. Chatillon, G. Ducrosa, and K. Froment. Thermodynamics of the O-U system. IV Critical assessment of chemical potentials in the U-$UO_{2.01}$ composition range. *J. Nucl. Mater.*, 349:17 – 56, 2006.

[3] M. Ben Saada. *Étude du comportement visco-plastique du dioxyde d'uranium*. PhD thesis, Université de Lorraine, 2017.

[4] M. Ben Saada, X. Iltis, N. Gey, B. Beausir, A. Miard, P. Garcia, and N. Maloufi. Influence of strain conditions on the grain sub-structuration in crept uranium dioxide pellets. *Journal of Nuclear Materials*, 518:265–273, 2019.

[5] P. T. Bretheau, J. Castaing, J. Rabier, and P. Veyssière. Mouvement des dislocations et plasticité à haute température des oxydes binaires et ternaires. *Advances in Physics*, 28(6):835–1014, 1979.

[6] P. T. Bretheau, C. Marhic, M. Spendel, and J. Castaing. Fluage à haute température de monocristaux d'oxyde cuivreux. *The Philosophical Magazine: A Journal of Theoretical Experimental and Applied Physics*, 35(6):1473–1487, 1977.

[7] B. Burton, G. L. Reynolds, and J. P. Barnes. The influence of grain size on the creep of uranium dioxide. *Journal of Materials Science*, 8(12):1690–1694, Dec 1973.

[8] Cabrera-Cano, J. and Castaing, J. Point defects and high temperature creep of NiO single crystals. *J. Physique Lett.*, 41(5):119–122, 1980.

[9] D. Caillard and J. Martin. Microstructure of aluminium during creep at intermediate temperatures—III. The rate controlling process. *Acta Metallurgica*, 31(5):813–825, 1983.

[10] A. Caneiro, M. Bonnat, and J. Fouletier. Measurement and regulation of oxygen content in selected gases using solid electrolyte cells. IV. Accurate preparation of CO2-CO and H2O-H2 mixtures. *Journal of Applied Electrochemistry*, 11(1):83–90, Jan 1981.

[11] W. R. Cannon and T. G. Langdon. Creep of ceramics. *Journal of Materials Science*, 23(1):1–20, Jan 1988.

[12] J. Chaboche. A review of some plasticity and viscoplasticity constitutive theories. *International Journal of Plasticity*, 24(10):1642–1693, 2008. Special Issue in Honor of Jean-Louis Chaboche.

[13] C. Colin. *Étude du fluage du dioxyde d'uranium*. PhD thesis, École Nationale supérieure des Mines de Paris, 2003.

[14] M. Cottura, Y. L. Bouar, A. Finel, B. Appolaire, K. Ammar, and S. Forest. A phase field model incorporating strain gradient viscoplasticity: Application to rafting in Ni-base superalloys. *Journal of the Mechanics and Physics of Solids*, 60(7):1243–1256, 2012.

[15] F. Dherbey. *Déformation à chaud du dioxyde d'uranium polycristallin : des mécanismes microscopiques au comportement macroscopique*. PhD thesis, Institut National Polytechnique de Grenoble, 2000.

[16] R. Dieckmann. Point defects and transport properties of binary and ternary oxides. *Solid State Ionics*, 12:1–22, 1984.

[17] A. DominguezRodriguez, M. Sanchez, R. Marquez, J. Castaing, and C. Monty. Point defects and high temperature creep of CoO single crystals. *Journal de Physique, Colloque C3*, 42:67–72, June 1981.

[18] B. Dorado, D. A. Andersson, C. R. Stanek, M. Bertolus, B. P. Uberuaga, G. Martin, M. Freyss, and P. Garcia. First-principles calculations of uranium diffusion in uranium dioxide. *Phys. Rev. B*, 86:035110, Jul 2012.

[19] J. Fouletier, H. Seinera, and M. Kleitz. Measurement and regulation of oxygen content in selected gases using solid electrolyte cells. II. Differential gauge. *Journal of Applied Electrochemistry*, 5(3):177–185, Aug 1975.

[20] C. Frederick and P. Armstrong. A mathematical representation of the multiaxial Bauschinger effect. Technical Report RD/B/N731, Central ELectricity Generating Board, Berkeley, UK, 1966.

[21] P. Garcia, E. Pizzi, B. Dorado, D. Andersson, J. Crocombette, C. Martial, G. Baldinozzi, D. Siméone, S. Maillard, and G. Martin. A defect model for UO2+x based on electrical conductivity and deviation from stoichiometry measurements. *Journal of Nuclear Materials*, 494:461–472, 2017.

[22] T. Helfer, S. Bejaoui, and B. Michel. Licos, a fuel performance code for innovative fuel elements or experimental devices design. *Nuclear Engineering and Design*, 294:117–136, 2015.

[23] T. Helfer, B. Michel, J.-M. Proix, M. Salvo, J. Sercombe, and M. Casella. Introducing the open-source mfront code generator: Application to mechanical behaviours and material knowledge management within the

PLEIADES fuel element modelling platform. *Computers & Mathematics with Applications*, 70(5):994–1023, 2015.

[24] R. Keller, T. Mitchell, and A. Heuer. Plastic deformation in nonstoichiometric UO2 + x single crystals—II. Deformation at high temperatures. *Acta Metallurgica*, 36(4):1073–1083, 1988.

[25] S. M. Keralavarma, T. Cagin, A. Arsenlis, and A. A. Benzerga. Power-Law Creep from Discrete Dislocation Dynamics. *Phys. Rev. Lett.*, 109:265504, Dec 2012.

[26] Kofstad Per. *Nonstoichiometry, diffusion, and electrical conductivity in binary metal oxides*. New York (N.Y.) : Wiley-Interscience, 1972.

[27] T. G. Langdon. Grain boundary sliding as a deformation mechanism during creep. *The Philosophical Magazine: A Journal of Theoretical Experimental and Applied Physics*, 22(178):689–700, 1970.

[28] H. Mansour, M. Crimp, N. Gey, X. Iltis, and N. Maloufi. Dislocation analysis of a complex sub-grain boundary in UO2 ceramic using accurate electron channelling contrast imaging in a scanning electron microscope. *Ceramics International*, 45(15):18666–18671, 2019.

[29] T. Markin and R. Bones. . Report AERE-4178, 1962.

[30] H. Matzke. Atomic transport properties in UO2 and mixed oxides (U,Pu)O2. *J. Chem. Soc., Faraday Trans. 2*, 83:1121–1142, 1987.

[31] C. Miehe, S. Goktepe, and J. M. Diez. Finite viscoplasticity of amorphous glassy polymers in the logarithmic strain space. *International Journal of Solids and Structures*, 46(1):181–202, 2009.

[32] J. Philibert. Creep and diffusion. *Solid State Ionics*, 12:321–336, 1984.

[33] J.-P. Poirier. *Creep of Crystals: High-Temperature Deformation Processes in Metals, Ceramics and Minerals*. Cambridge Earth Science Series. Cambridge University Press, 1985.

[34] M. B. Saada, N. Gey, B. Beausir, X. Iltis, H. Mansour, and N. Maloufi. Sub-boundaries induced by dislocational creep in uranium dioxide analyzed by advanced diffraction and channeling electron microscopy. *Materials Characterization*, 133:112–121, 2017.

[35] M. Salvo, J. Sercombe, J.-C. Ménard, J. Julien, T. Helfer, and T. Désoyer. Experimental characterization and modelling of UO2 behavior at high temperatures and high strain rates. *Journal of Nuclear Materials*, 456:54–67, 2015.

[36] M. Seltzer, A. Clauer, and B. Wilcox. The stress dependence for high temperature creep of polycrystalline uranium dioxide. *Journal of Nuclear Materials*, 34(3):351–353, 1970.

[37] M. Seltzer, A. Clauer, and B. Wilcox. The influence of stoichiometry on compression creep of polycrystalline UO2+x. *Journal of Nuclear Materials*, 44(3):331–336, 1972.

[38] C. Vivant-Duguay. *Contribution à l'étude du fluage du dioxyde d'uranium.* PhD thesis, Institut National des Sciences Appliquées de Lyon, 1998.

[39] J. Weertman. Theory of steady–state creep based on dislocation climb. *Journal of Applied Physics*, 26(10):1213–1217, 1955.

[40] J. Weertman. Dislocation climb theory of steady state creep. volume 61, pages 681–694, 1968.

[41] J. Weertman. Natural fifth creep law for pure metals. Number pt 1, pages 1–13, 1984.

[42] V. Wheeler and I. Jones. Thermodynamic and composition changes in UO2±x (x¡ 0.005) at 1950 K. *Journal of Nuclear Materials*, 42(2):117–121, 1972.

[43] M. H. Yoo and H. Trinkaus. Crack and cavity nucleation at interfaces during creep. *Metallurgical Transactions A*, 14(3):547–561, Mar 1983.